

Available online at [www.sciencedirect.com](http://www.sciencedirect.com)

**jmr&t**  
Journal of Materials Research and Technology

journal homepage: [www.elsevier.com/locate/jmrt](http://www.elsevier.com/locate/jmrt)

# Investigations on the oxidation behavior and removal mechanism of SiC/SiC composites by multi-pulse femtosecond laser ablation



Ning Zhou <sup>a</sup>, Songmei Yuan <sup>a,b,\*</sup>, Mengxuan Gao <sup>a</sup>, Wei Zhang <sup>c</sup>,  
Jiaqi Zhang <sup>a</sup>, Tianrui Hu <sup>a</sup>

<sup>a</sup> R&D Center of High-efficient & Green CNC Machining Technology and Equipment, School of Mechanical Engineering and Automation, Beihang University, Beijing, 100191, China

<sup>b</sup> Ningbo Institute of Technology, Beihang University, Ningbo, 315832, China

<sup>c</sup> National Key Laboratory of Science and Technology on Power Beam Processes, AVIC Aeronautical Manufacturing Technology Research Institute, Beijing, 100024, China

## ARTICLE INFO

### Article history:

Received 3 May 2023

Accepted 15 August 2023

Available online 19 August 2023

### Keywords:

SiC/SiC composites  
Multi-pulse femtosecond laser  
Oxidation behavior  
Removal mechanism  
Heat accumulation effect

## ABSTRACT

SiC/SiC (SiC fiber-reinforced SiC matrix) composites have superior performance, making them promising candidates as one of the best materials for high-temperature components in aerospace applications. This investigation analyzed the morphology, structure, composition, and plasma state of multi-pulse femtosecond laser ablated SiC/SiC composites from multiple perspectives using various static and in situ characterization methods. Further, the oxidation behavior and removal mechanism of SiC/SiC composites were studied qualitatively and quantitatively. The results indicated that the ablation products of multi-pulse femtosecond laser ablation of SiC/SiC composites were mainly SiO<sub>2</sub> and plasma deposits. The heat accumulation effect and oxidation degree at the ablation locations were enhanced accordingly as the effective ablation number or energy density increased, and the main shape of the products also changed regularly. At the same time, the material removal mechanism changed from non-thermal removal dominated to the equilibrium stage and then to thermal removal dominated. The detailed analysis of the oxidation behavior of each component in SiC/SiC composites enabled the controlled ablation of femtosecond lasers targeting the oxidation process of SiC/SiC composites. Besides, 1 MPa N<sub>2</sub> could improve the processing efficiency of femtosecond laser for the depth and width of the groove by a maximum of about 90.40% and 104.02% in this study, respectively. Ultimately, the range of laser process parameters corresponding to multi-pulse femtosecond laser ablation of SiC/SiC composites without thermal removal as dominant was determined.

© 2023 The Author(s). Published by Elsevier B.V. This is an open access article under the CC BY-NC-ND license (<http://creativecommons.org/licenses/by-nc-nd/4.0/>).

\* Corresponding author. R&D Center of High-efficient & Green CNC Machining Technology and Equipment, School of Mechanical Engineering and Automation, Beihang University, Beijing, 100191, China.

E-mail address: [yuansmbuaa@163.com](mailto:yuansmbuaa@163.com) (S. Yuan).

<https://doi.org/10.1016/j.jmrt.2023.08.134>

2238-7854/© 2023 The Author(s). Published by Elsevier B.V. This is an open access article under the CC BY-NC-ND license (<http://creativecommons.org/licenses/by-nc-nd/4.0/>).

## 1. Introduction

With the rapid development of aerospace technology, the demands for the performance of high-temperature-resistant components are increasing [1]. It is difficult to significantly raise the ultimate working temperature of conventional superalloys, resulting in the advantages of new high-temperature-resistant ceramic matrix composites becoming increasingly apparent [2]. Continuous SiC fiber-reinforced SiC matrix (SiC/SiC) composites stand out for their low density, high-temperature resistance, corrosion resistance, and excellent mechanical performance [3,4]. SiC/SiC composites are one of the best alternative materials for hot-end components of aeronautics turbine engines and aeronautics high-temperature protection components due to their exceptional properties [5]. Nevertheless, high hardness, weak conductivity, severe anisotropy, and inhomogeneity make the SiC/SiC composites challenging to be processed [6]. During traditional mechanical processing, the process would accompany cracks, delamination, fiber pull-out, and other flaws [7]. Furthermore, the processing of SiC/SiC composites using non-traditional processing methods, such as ultrasonic vibration and water jet, is restricted due to glaring processing defects and low precision [8,9]. As a result, there is an urgent requirement to develop processing methods with high efficiency, low damage, and excellent accuracy for the engineering and manufacturing of SiC/SiC composites in aerospace structural components.

The femtosecond laser has an ultra-short pulse width and an ultra-high peak energy density. The femtosecond laser is extensively utilized in fabricating components from difficult-to-machine materials because of its excellent processing precision, low thermal influence, and non-contact stress [10]. Consequently, femtosecond laser processing of SiC/SiC composites is a vital research direction in aerospace. Zhai et al. [11] processed SiC/SiC composites with a high-frequency femtosecond laser. The results showed that surface oxidation was an essential defect in the processing and that controlling the morphology required changing the process parameters. Liu et al. [12] used a femtosecond laser with different parameters to perforate SiC/SiC composites. The results showed that the spot overlap rate substantially impacted the quality and depth of the holes and that increasing power would improve the surface quality and processing outcomes. Yan et al. [13] polished SiC/SiC composites with a femtosecond laser and utilized finite element analysis to establish the related theoretical model. The results indicated that surface oxidation and defects decreased considerably when the incidence angle increased, and the resonance enhancement effect of laser energy was successfully predicted. Liu et al. [14] used the filament effect of the femtosecond laser to punch holes in SiC/SiC composites, and the findings demonstrated that varied punching methods significantly impact hole depth. The above studies confirmed the feasibility of femtosecond laser high-precision processing of SiC/SiC composites.

However, most current studies on femtosecond laser processing of SiC/SiC composites have mainly focused on the effects of process parameters on material morphology and structure, with less attention paid to the oxidation behavior

and removal mechanism of SiC/SiC composites. In addition, the heat accumulation of the multi-pulse femtosecond laser at the ablation locations in specific cases is not negligible. Moreover, improving the processing efficiency of the femtosecond laser and revealing the interaction mechanism between the femtosecond laser and material are urgent challenges in engineering and research. Therefore, this paper aims to analyze the morphology, structure, composition, and plasma state of SiC/SiC composites via multi-pulse femtosecond laser processing using different effective ablation numbers and energy densities as well as with or without nitrogen to gain a deeper understanding of the oxidation behavior and removal mechanism of SiC/SiC composites ablated by the multi-pulse femtosecond laser. To lay a solid foundation for high efficiency, low damage, and high precision processing of SiC/SiC composites by femtosecond laser and to reveal the interaction mechanism between femtosecond laser and material at the atomic level.

## 2. Experimental

### 2.1. Materials

This research used two-dimensional (2D) structured SiC/SiC composites (Central South University, China) prepared through the melt infiltration (MI) process. The SiC/SiC composites prepared by the MI process have low porosity (~2%), and the material matrix contains about 20 vol% of unreacted free-state silicon. Therefore, the matrix of the SiC/SiC composites used in this study was mainly a two-phase mixture of SiC and Si. The left side of Fig. 1(a) shows the schematic structure of 2D SiC/SiC composites. Its main structures include SiC and Si material matrix, SiC fibers oriented at 0° and 90°, and the interface layer between the fiber and the matrix. Among them, the main component of the interface layer is pyrolytic carbon (PyC). The macroscopic reinforcing phase of the material is formed by flattening and laminating fiber bundles composed of SiC fibers. The scanning electron microscope (SEM) image of the cross-section of the SiC fiber bundle is shown on the right side of Fig. 1(a), which can observe the distribution state of the matrix, fibers, and interface layers. Table 1 illustrates the primary characteristic parameters of SiC/SiC composites.

### 2.2. Femtosecond laser equipment

Fig. 1(b) shows the schematic diagram of the machining system for multi-pulse femtosecond laser ablation of SiC/SiC composites. The machining system mainly contains a laser output and three-axis computer numerical control (CNC) systems. The laser output system is a Yb:KGW all-solid-state femtosecond laser (PH1-20, Light Conversion, Lithuania) that uses the chirped pulse amplification technique. This research used a 1030 nm fs laser to ablate SiC/SiC composites based on the wavelength of the output light source. The three-axis CNC system consists mainly of nanoscale linkage stages (ANT95XY, Aerotech, America). The laser is focused using a convex lens with a focal length  $f$  of 150 mm. A coaxial blowing system can control the use of 1 MPa N<sub>2</sub> as an auxiliary gas. The

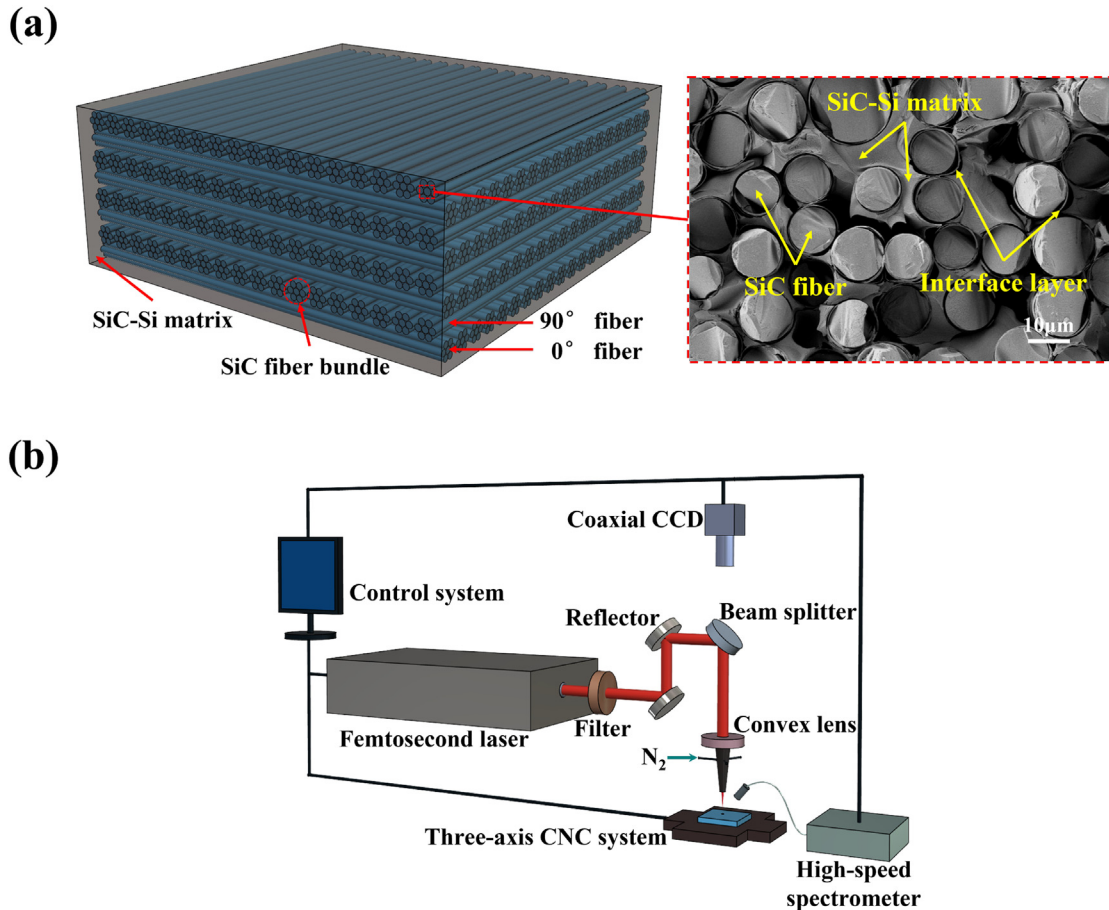


**Fig. 1 – (a)** Schematic structure of 2D SiC/SiC composites and SEM image of the cross-section of the SiC fiber bundle. **(b)** Schematic diagram of the machining system for multi-pulse femtosecond laser ablation of SiC/SiC composites.

**Table 1 – Primary characteristic parameters of SiC/SiC composites.**

Parameter	Unit	Value
Density	g/cm <sup>3</sup>	2.2
Diameter of SiC fiber	μm	10–20
Thickness of interface layer	nm	200–400
Fiber volume fraction	\	40%
Layer volume fraction	\	0.2%
Porosity	\	2%
Size	mm <sup>3</sup>	30 × 30 × 4

processing of the material can be observed in real-time with a coaxial charge-coupled device (CCD) camera.

### 2.3. Experimental procedure

**Table 2** illustrates the primary technological parameters for multi-pulse femtosecond laser ablate SiC/SiC composites. In this paper, a multi-pulse femtosecond laser was used to process groove structure on the surface of SiC/SiC composites under different effective ablation numbers and energy densities, as well as with or without nitrogen. To remove most impurities from the surface of the SiC/SiC composites, the researchers ultrasonically cleaned the material with 75%

alcohol prior to laser processing, then rinsed with deionized water and dried it. The multi-pulse femtosecond laser grooving experiments were mainly performed on two groups of 2D SiC/SiC composite samples of the same size. Both groups of samples were subjected to orthogonal experiments using different scanning numbers and energy densities, as in **Table 2**. The same parameters were used at the corresponding positions on both groups of samples. The difference was that the first group sample did not use N<sub>2</sub>, while the second group used 1Mpa N<sub>2</sub>. It is worth mentioning that the inhomogeneity of 2D SiC/SiC composites and the complexity of their composition lead to the fact that the two groups of samples will not be identical.

In this study, multi-pulse femtosecond laser processing was the cumulative effect of a multi-shot laser on SiC/SiC composites. The relationship between the effective ablation number N<sub>e</sub> and the scanning speed V<sub>s</sub> of the femtosecond laser pulse is as follows [15]:

$$N_e = \sqrt{\frac{\pi}{2}} \frac{2w_0 v}{V_s} \quad (1)$$

where w<sub>0</sub> is the focal spot radius of the laser and v is its repetition frequency. According to the calculation in **Tables 2** and it is obtained that N<sub>e</sub> is about 7520 times when the scanning number is 1. Since the time interval between different

**Table 2 – Primary technological parameters for multi-pulse femtosecond laser ablate SiC/SiC composites.**

Parameter	Symbol	Unit	Value
Wavelength	$\lambda$	nm	1030
Maximum average power	P	W	20
Pulse width	$t_p$	fs	290
Maximum single pulse energy	$E_p$	μJ	200
Repetition frequency	v	kHz	100
Focal spot radius (in air)	$w_0$	μm	30
Scanning speed	$V_s$	mm/s	1
Beam quality	✓	✓	TEM <sub>00</sub> ( $M^2 < 1.2$ )
Polarization	✓	✓	Linear
Scanning number	N	✓	1/5/10/20
Energy Density	F	J/cm <sup>2</sup>	1.77/3.54/5.31/7.07

scans of the same path was extremely short in this study, the effective ablation number of laser pulses corresponding to the N scan was approximately  $N \cdot N_e$ .

#### 2.4. Characterization

The depth and width of the grooves were measured using an ultra depth of field 3D microscopic (3DM, VHX-5000, Keyence, Japan). A scanning electron microscope (ZEISS Gemini 300, Carl Zeiss AG, Germany) was utilized to observe the typical morphology of the material before and after processing. In addition, energy dispersive spectroscopy (EDS) was employed to determine the atomic percentage of each element on the material's surface. An X-ray diffractometer (XRD, Empyrean, Panalytical, Netherlands) was used to analyze the phase and crystal structure of the material via Cu K $\alpha$  radiation ( $\lambda = 1.541 \text{ \AA}$ ). X-ray photoelectron spectroscopy (XPS, ESCALAB 250Xi, Thermo Fisher Scientific, America) with monochromatic Al K $\alpha$  (1486.6 eV) X-ray radiation was utilized to detect changes in element species and chemical bond content on the sample surface before and after processing. The material surface was not etched with an Ar $^+$  ion beam prior to XPS detection. The C1s peak (BE = 284.8 eV) was utilized for charge calibration of the XPS spectrum. The composition

change of the material was investigated using a laser confocal Raman spectrometer (Raman, LabRAM HR Evolution, Horiba Scientific, France) before and after processing at room temperature. The state of the plasma generated during femtosecond laser ablation of SiC/SiC composites was detected in situ using a high-speed plasma spectrometer (AvaSpec-ULS2048CL-EVO, Avantes, Netherlands). The above tests were performed on SiC/SiC composite samples due to the limited amount of the products on the samples, which did not support the collection detection.

### 3. Results and discussion

#### 3.1. Physical phase

First, the overall machined surface of SiC/SiC composite samples after multi-pulse femtosecond laser processing was analyzed in the phase. The XRD results of the machined surfaces of SiC/SiC composites before multi-pulse femtosecond laser processing without N<sub>2</sub> and with 1 Mpa N<sub>2</sub> are shown at the bottom of Fig. 2(a and b), respectively. As shown in the figure, the diffraction peaks at 35.6°, 41.4°, 60.0°, 71.8°, and 75.5° corresponded to (111), (200), (220),

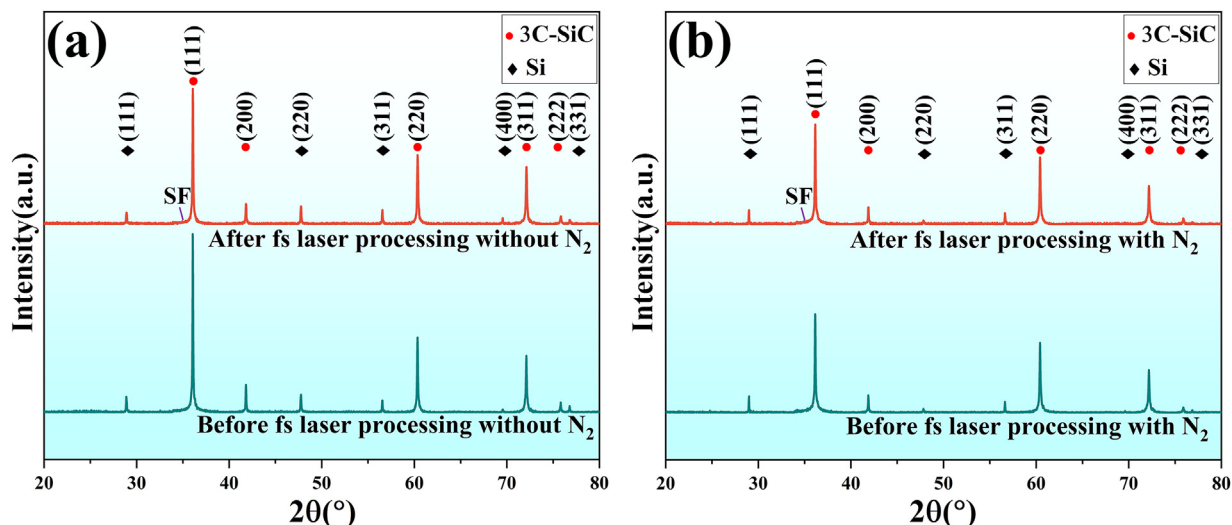


**Fig. 2 – XRD results of the machined surfaces of SiC/SiC composites before and after multi-pulse femtosecond laser processing: (a) without N<sub>2</sub>, (b) with N<sub>2</sub>.**

(311), and (222) crystal planes of polycrystalline 3C–SiC (JCPDS Card No.29-1129) [16]. The sharpness of the diffraction peaks demonstrated the high crystallinity of 3C–SiC in SiC/SiC composites. In addition, 3C–SiC featured a face-centered cubic structure corresponding to the F-43m(216) space group. Extremely low-intensity diffraction peaks frequently arise around 33.6° in the XRD results of 3C–SiC, primarily due to stacking faults inside the 3C–SiC crystal [17]. The diffraction peaks at 28.4°, 47.3°, 56.1°, 69.2°, and 76.4° corresponded to (111), (220), (311), (400), and (331) crystal planes of polycrystalline Si (JCPDS Card No. 27–1402) [18]. The sharpness of the diffraction peaks likewise revealed that the crystallinity of free Si in SiC/SiC composites was also relatively high. The free Si also had a face-centered cubic structure corresponding to the Fd3m(227) space group. Comparing the XRD results of the two groups of raw materials, it could be seen that the composition of the two groups of samples was the same. At the same time, the difference in peak intensity at the same position could be attributed to the inhomogeneity of the SiC/SiC composites.

The XRD results of the machined surfaces of the two groups of SiC/SiC composite samples after multi-pulse femtosecond laser processing are shown at the top of Fig. 2(a and b), respectively. As shown in the figure, the position and intensity of the diffraction peaks did not change significantly after undergoing femtosecond laser orthogonal experiments on both groups of SiC/SiC composite samples compared to before processing, regardless of whether N<sub>2</sub> was used. It was noticeable that the diffraction peak of SiO<sub>2</sub> did not appear near 21.3° [19], and no other new phase was detected. As a matter of experience, the substances with the content below about 5% are exceedingly difficult to obtain the corresponding diffraction peaks in XRD detection (especially for the amorphous phase). Therefore, it could be determined from the above XRD results that no significant phase change occurred in the SiC/SiC composite samples after multi-pulse femtosecond laser processing, provided that the generation of trace new phases cannot be excluded. Comparing with the presence of significant diffraction peaks of SiO<sub>2</sub> in XRD results after continuous laser processing of SiC/SiC composites in related studies [20], it showed the relatively low thermal effect of multi-pulse femtosecond laser processing of SiC/SiC composites in this study. However, the limitation of the detection accuracy of XRD made it necessary to confirm whether small amounts of oxides were formed in SiC/SiC composites after multi-pulse femtosecond laser processing in combination with other high-sensitivity detections in this study.

### 3.2. Morphology

Since the structure of the grooves was symmetrical, this study focused on the morphology of one side of the grooves under each set of parameters on the sample. The SEM images of the groove morphology obtained by multi-pulse femtosecond laser processing on two groups of SiC/SiC composite samples under different effective ablation numbers and energy densities, as well as with or without nitrogen, were shown in Fig. 3. As shown in the figure, the morphology of the grooves

shows regular changes with the gradual increase of the effective ablation number or energy density.

Firstly, the first group sample without N<sub>2</sub> was analyzed in detail. As shown in Fig. 3(a1-4), when the laser energy density was 1.77 J/cm<sup>2</sup>, with the increasing effective ablation number, the ablation position first appeared flocculent accumulation, followed by block accumulation. A small amount of recasts was produced when the effective ablation number reached 10N<sub>e</sub>. Recasts were formed because molten materials converge and solidify under the action of liquid surface tension. The recasts obtained in this study were consistent with the morphology and structure of the recasts appearing on SiC/SiC composites reported by Cai et al. [21]. Moreover, as the effective ablation number continued to increase to 20N<sub>e</sub>, the volume of the recasts increased accordingly. According to several studies [22–24] on the heat accumulation effect due to the accumulation of femtosecond laser pulses, it was known that there was a certain heat accumulation effect of multi-pulse femtosecond laser ablated SiC/SiC composites. The heat accumulation effect changed with the increase of the effective ablation number, affecting the main shape of the products.

Further, as shown in Fig. 3(b1-d4), when the energy densities were 3.54, 5.31, and 7.07 J/cm<sup>2</sup>, respectively, the heat accumulation effect was known to be gradually enhanced with the increase of the effective ablation number based on the volume of recasts at the ablation locations. As shown in Fig. 3(a1-d4), when the effective ablation numbers were 1N<sub>e</sub>, 5N<sub>e</sub>, 10N<sub>e</sub>, and 20N<sub>e</sub>, respectively, the trend of the main shape of the products with the increase of energy density was similar to that when the effective ablation number was increased. The above illustrated that when the effective ablation number was constant, the heat accumulation effect gradually enhanced with increased energy density. Therefore, the above results demonstrated that the heat accumulation effect due to the accumulation of femtosecond laser pulses enhanced with the effective ablation number or energy density when no N<sub>2</sub> was used.

Secondly, the second group sample using 1 Mpa N<sub>2</sub> was analyzed in detail. As shown in Fig. 3(e1-h4), the morphology at the ablation locations of the second group sample also showed a regular variation. With the increase of the effective ablation number or energy density, the main shape of the products was from flocculent to block. Importantly, no recasts were present at the ablation locations. Combined with the analytical results of the first group sample, using 1 Mpa N<sub>2</sub> with the same parameters could effectively reduce the heat accumulation effect and thus avoid the generation of recasts. In addition, the ablation results of the femtosecond laser need to be analyzed in more depth with the structure, composition, typical morphology, and plasma state.

### 3.3. Structure

After multi-pulse femtosecond laser processing, the structure of the grooves was analyzed for both groups of samples. The recasts were removed from the edge of the groove by mechanical stripping prior to measuring the depth and width of the grooves using 3DM. The variation of the depth and width on both groups of samples with different process parameters

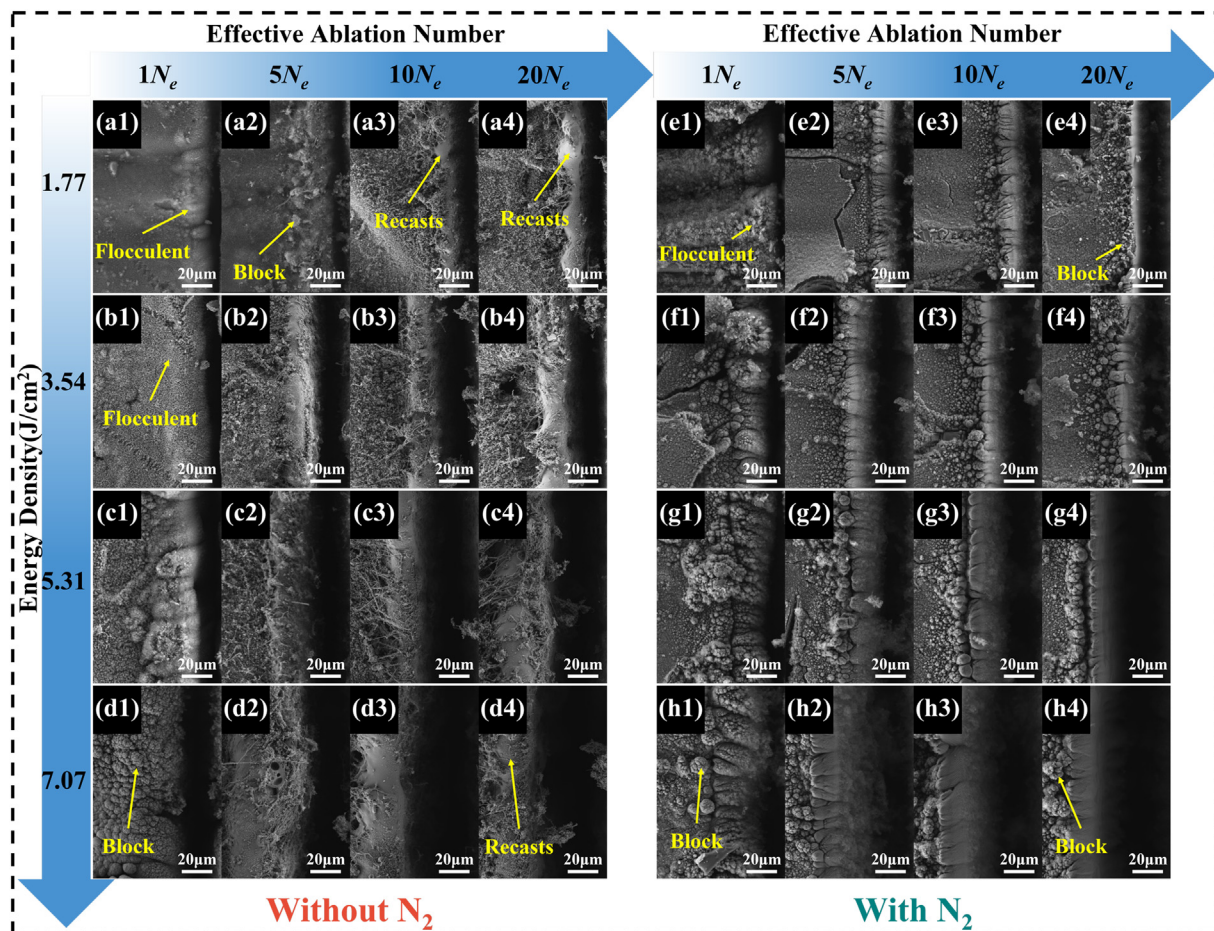


**Fig. 3 – SEM images of the groove morphology obtained by multi-pulse femtosecond laser processing on two groups of SiC/SiC composite samples under different effective ablation numbers and energy densities: (a1-d4) without N<sub>2</sub>, (e1-h4) with N<sub>2</sub>.**

are shown in Fig. 4, respectively. As can be seen from the figures, the overall trend of the depth and width of each groove on both groups of samples gradually increased with the increase of the effective ablation number or energy density. However, there were differences in the growth rate between the data groups.

On the one hand, as shown in Fig. 4(a), the growth rate of the depth with the increase of the effective ablation number is gradually slowed down at different energy densities in the first group sample. That was because as the depth increased, it became more difficult for the plasma and the products to escape from the groove. Further, a large amount of plasma was generated and gathered. The plasma absorbed part of the laser energy by inverse bremsstrahlung, creating a plasma shielding effect that made it difficult for the laser energy to reach the bottom of the groove. As shown in Fig. 4(b), on the second group sample using N<sub>2</sub>, the growth rate of the depth also gradually slows down as the effective number of ablations increases. However, it is greater than on the first group sample at the same parameters. It was because high-pressure N<sub>2</sub> made it easier for the plasma and products to escape from the interior of grooves, reducing the plasma shielding effect, which improved the efficiency and capability of femtosecond laser. As shown in Fig. 4(c and d), the growth rate of groove

depth on both groups of samples did not slow down significantly with increasing energy density.

On the other hand, as shown in Fig. 4(e–h), the growth rate of groove width on both groups of samples became progressively slower as the effective ablation number or energy density increased, with or without nitrogen. It could be attributed to the limited spot size and the removal threshold effect of the femtosecond laser on the material. Similarly, the width of the grooves obtained with high-pressure nitrogen was greater than that obtained without it at the same parameters. Therefore, in this study, the depth and width of the grooves could be increased by increasing the effective ablation number or energy density. However, given the influence of the heat accumulation effect, appropriate process parameters should be selected. By calculating the data in Fig. 4, it could be seen that using 1 MPa N<sub>2</sub> in this study could improve the processing efficiency of the femtosecond laser for the depth and width of the grooves by a maximum of about 90.40% and 104.02%, respectively.

### 3.4. Composition

Regarding the compositional analysis of SiC/SiC composites at the ablation locations before and after multi-pulse

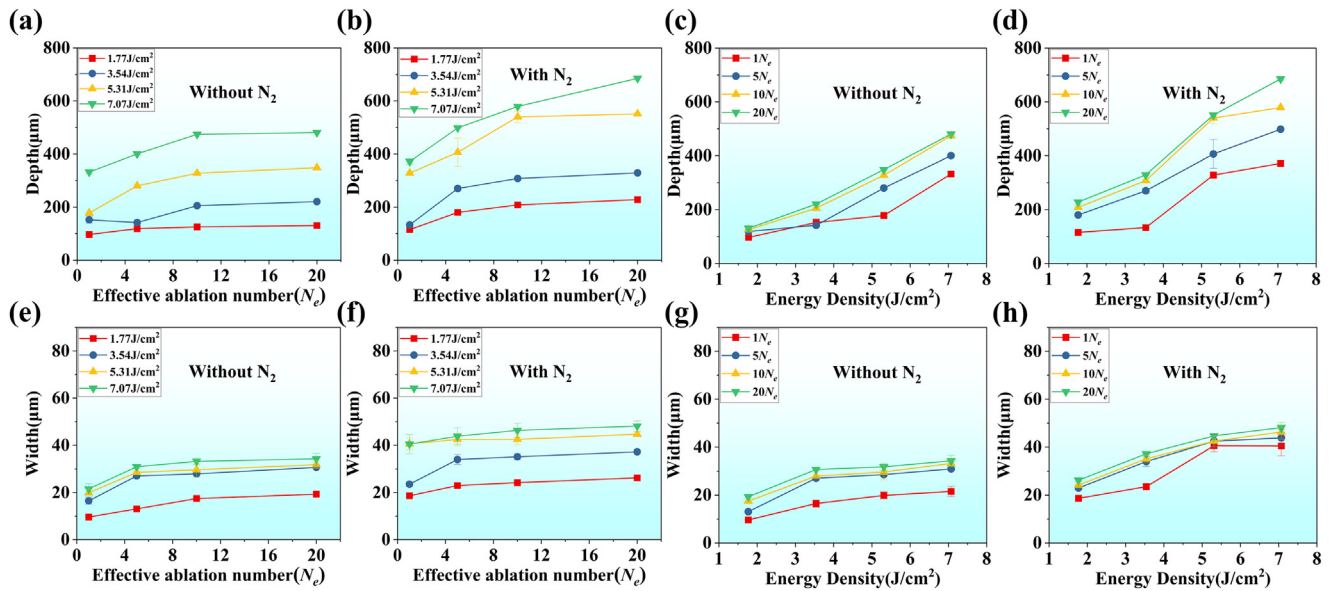


**Fig. 4 – Variation of the depth and width of the grooves on both groups of samples with different effective ablation numbers and energy densities.**

femtosecond laser processing, X-ray photoelectron spectroscopy detection can characterize the changes in elemental species and chemical bonding content on the sample surface. The ablation positions corresponding to Fig. 3(d4) and Fig. 3(h4) were selected on both groups of samples, namely the two ablation positions when the effective ablation number was  $20N_e$ , and the energy density was  $7.07 \text{ J/cm}^2$ . Three detection points were taken at 0.3 mm, 0.6 mm, and 0.9 mm from the central axis of the two grooves and set to positions 1 to 6, respectively. The XPS results of the six detection positions on the SiC/SiC composites before and after the multi-pulse femtosecond laser processing are shown in Fig. 5.

Firstly, Fig. 5(a1,b1,c1) show the XPS spectra of the corresponding raw materials. The figures show that the main elements of the SiC/SiC composites at the ablation locations are Si, C, and O before multi-pulse femtosecond laser processing. The presence of O element in the raw material might be due to adsorbed impurities and the formation of trace oxide films on the surface of the material where weak oxidation occurred. As shown in Fig. 5(a1-7), comparing the intensity of the O1s peaks at six detection positions after multi-pulse femtosecond laser processing and the raw material, it could be seen that the multi-pulse femtosecond laser ablation caused a certain degree of oxidation on the SiC/SiC composites, and using N<sub>2</sub> could significantly inhibit the enhancement of the O1s peaks.

Secondly, Fig. 5(b1-7) showed the high-resolution Si2p spectra at the raw material and six detection positions. Based on the Gauss-Lorentz sum function assumption for each peak, the Si2p of the raw material consisted of Si–Si, Si–C, and Si–O peaks at 99.18 eV, 100.78 eV, and 103.03 eV, respectively [25,26]. The above three XPS peaks could be attributed to the Si–Si bond of free Si, the Si–C bond of polycrystalline 3C–SiC, and the Si–O bond of the surface

oxide films, respectively. As shown in Fig. 5(b2-4), the Si–Si and Si–C bonds no longer existed at the three detection positions in the first group sample relative to the Si2p spectrum of the raw material. In contrast, the Si–O bond content increased substantially. That illustrated that multi-pulse femtosecond laser processing caused Si–Si and Si–C bonds to break without N<sub>2</sub>. The broken chemical bonds combine with O to form many Si–O bonds, eventually deposited mainly as Si-containing solid oxides at the ablation locations. Further, as shown in Fig. 5(b5-7), a small decrease in the Si–Si and Si–C bond content and a slight increase in the Si–O bond content occurred at the three detection positions of the second group sample relative to the Si2p spectrum of the raw material. That also illustrated that using 1 MPa N<sub>2</sub> could effectively inhibit the Si–Si and Si–C bonds oxidation to Si–O bonds caused by multi-pulse femtosecond laser ablation, thus reducing the generation of Si-containing solid oxides.

At last, Fig. 5(c1-7) showed the high-resolution C1s spectra at the raw material and six detection positions. The C1s of the raw material had C–Si, C–C, and C–O peaks at 283.86 eV, 284.77 eV, and 286.20 eV, respectively [27,28]. They could be attributed to the C–Si bond of polycrystalline 3C–SiC, the C–C bond of PyC, and the C–O bond of surface impurities in SiC/SiC composites. As shown in Fig. 5(c2-4), the C–Si bonds disappeared in the first group sample relative to the C1s spectrum of the raw material. The content of C–C bonds decreased dramatically, and more importantly, the XPS peaks corresponding to other chemical bonds containing C were not enhanced. It illustrated that multi-pulse femtosecond laser processing caused C–C and C–Si bonds to break without N<sub>2</sub>, combining with O to form CO<sub>2</sub> or CO and Si–O bonds. Eventually, CO<sub>2</sub> and CO escaped leading to a lower C atom content in the material. Further, as shown in Fig. 5(c5-7), the C–Si and C–C bond content was slightly reduced at three detection positions for the second group sample relative to the C1s

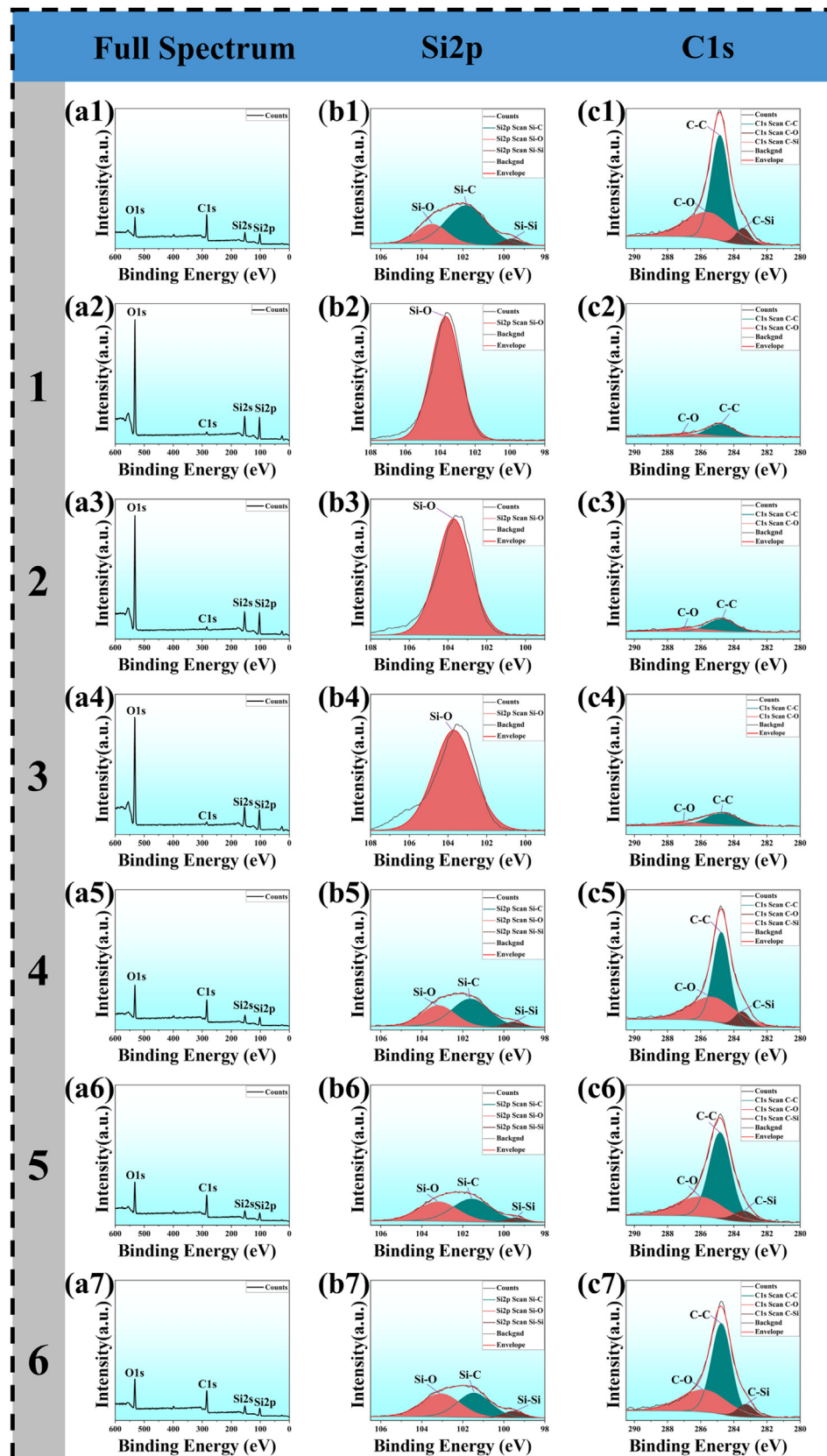


Fig. 5 – XPS results of raw material and six detection positions before and after multi-pulse femtosecond laser processing: (a1-7) full XPS spectrums, (b1-7) high-resolution Si2p spectrums, and (c1-7) high-resolution C1s spectrums.

spectrum of the raw material. Again, 1 MPa N<sub>2</sub> could effectively inhibit the C–Si and C–C bonds oxidation to Si–O bonds, CO<sub>2</sub>, or CO caused by multi-pulse femtosecond laser ablation. Several previous studies have demonstrated the oxidation of SiC/SiC composites due to high temperatures during laser processing [11,20]. Therefore, the oxidation of SiC, Si, and PyC could be attributed to high temperatures caused by heat accumulation effects in this study.

In addition, in the first group sample without N<sub>2</sub>, the O1s and Si–O peaks were stronger, and the C–C peaks were weaker at the closer detection position to the center of the grooves, mainly attributed to the higher oxidation degree as they were closer to the ablation center. In the second group sample with N<sub>2</sub>, the O1s, Si2p, and C1s peaks at different positions were not significantly different. It might be due to the low oxidation degree when using N<sub>2</sub>.

Furthermore, the compositional changes of SiC/SiC composites at the ablation locations before and after multi-pulse femtosecond laser processing were analyzed more in-depth with a laser confocal Raman spectrometer. The ablation position corresponding to Fig. 3(h1) is selected on the second group samples, that is, the ablation position with an effective ablation number of 1N<sub>e</sub> and an energy density of 7.07 J/cm<sup>2</sup> when using N<sub>2</sub>. One detection point is taken at 0.5 mm from the central axis of the grooves.

On the one hand, the lower part of Fig. 6 shows the Raman spectroscopy results for the raw materials, with the appearance of the Raman peaks of 3C–SiC, Si, and C, respectively. The first-order Raman scattering of polycrystalline 3C–SiC consists of relatively strong full triplet transverse optical (TO) phonon modes and relatively weak longitudinal optical (LO) phonon modes [29–31]. The positions 796 cm<sup>-1</sup> and 972 cm<sup>-1</sup> in the present results corresponded to the TO and LO phonon mode Raman peaks of polycrystalline 3C–SiC in SiC/SiC composites, respectively [32,33]. The asymmetry between the TO and LO phonon mode Raman peaks could be attributed to the internal stresses and the inherent stacking faults in the

3C–SiC matrix [16]. This result was consistent with the results of XRD regarding stacking faults in 3C–SiC. The stronger first-order transverse optical (TO) phonon mode and weaker two transverse optical (2TO) phonons mode Raman peaks at 520 cm<sup>-1</sup> and 950 cm<sup>-1</sup> corresponded to free Si, respectively [34,35]. The two weak Raman peaks at 1333 cm<sup>-1</sup> and 1596 cm<sup>-1</sup> corresponded to the D and G bands of carbon, respectively [29,36]. The D band was similar to the TO mode Raman peak of diamond (1340 cm<sup>-1</sup>), indicating the presence of C–C sp<sup>3</sup> bonds in 3C–SiC, while the G band was associated with sp<sup>2</sup> bonds in the graphite structure and could be attributed to PyC in the interface layer of SiC/SiC composites [37].

On the other hand, the upper part of Fig. 6 shows the Raman spectroscopy results for the sample detection location after laser processing. As shown in the figure, relative to the raw material, the intensities of the corresponding Raman peaks of both 3C–SiC and Si were drastically reduced after laser processing, while the Raman peaks of C were not significantly changed. Importantly, a weak Raman peak appeared near 916 cm<sup>-1</sup>, and several studies [31,38–40] have confirmed that it corresponded to amorphous SiO<sub>2</sub>. Therefore, combined with the XPS analysis results, it could be seen that the multi-pulse femtosecond laser ablation of SiC/SiC composites caused the oxidation of SiC and Si, and the resulting Si-containing solid oxide was amorphous SiO<sub>2</sub>.

### 3.5. Removal mechanism and oxidation behavior

The SEM images and the corresponding EDS surface scans of the SiC/SiC composites before multi-pulse femtosecond laser processing are shown in Fig. 9(a1,d1), respectively. As could be seen from the figure, SiC fibers appeared on the surface of the 2D SiC/SiC composites in addition to the matrix consisting of SiC and Si. The higher atomic ratio of C than Si in the EDS results for the raw material could be attributed to the PyC on the exposed SiC fibers. The atomic ratio of O in the raw material was 2.59%, caused by the trace oxide films and impurities on the material surface. The inhomogeneity of the SiC/SiC composites prepared by the MI process and the complexity of their composition resulted in no clear proportional relationship between the atomic ratio of Si and C in the raw material.

Fig. 7 corresponds to the statistical plot of the EDS surface scans for each ablation location in Fig. 3. As shown in the figure, with the gradual increase of the experiment parameters, the atomic ratio of O, C, and Si at the ablation locations of the two groups of samples also show regular changes. As the effective ablation number or energy density increased, the atomic ratio of O increased for both groups of samples. In contrast, the atomic ratio of C decreased, and the atomic ratio of Si fluctuated within a certain range. As shown in Fig. 7 (a1, b1, c1, d1), the atomic ratio of O compared to the raw material illustrated that different degrees of oxidation occurred at the ablation locations for each process parameter on both groups of samples. Moreover, the oxidation degree gradually increased as the effective ablation number or energy density increased. The result confirmed that as the effective ablation number or energy density increased, the stronger the heat accumulation effect caused higher temperatures, leading to a stronger oxidation degree. As shown in Fig. 7(a2,b2,c2,d2), the

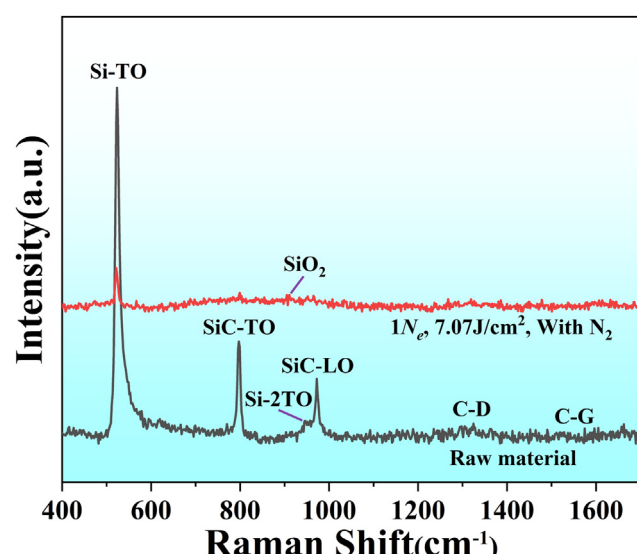


**Fig. 6 – Raman spectroscopy results: raw material and the second group of samples with energy densitiy of 7.07 J/cm<sup>2</sup> at an effective ablation number of 1N<sub>e</sub>.**

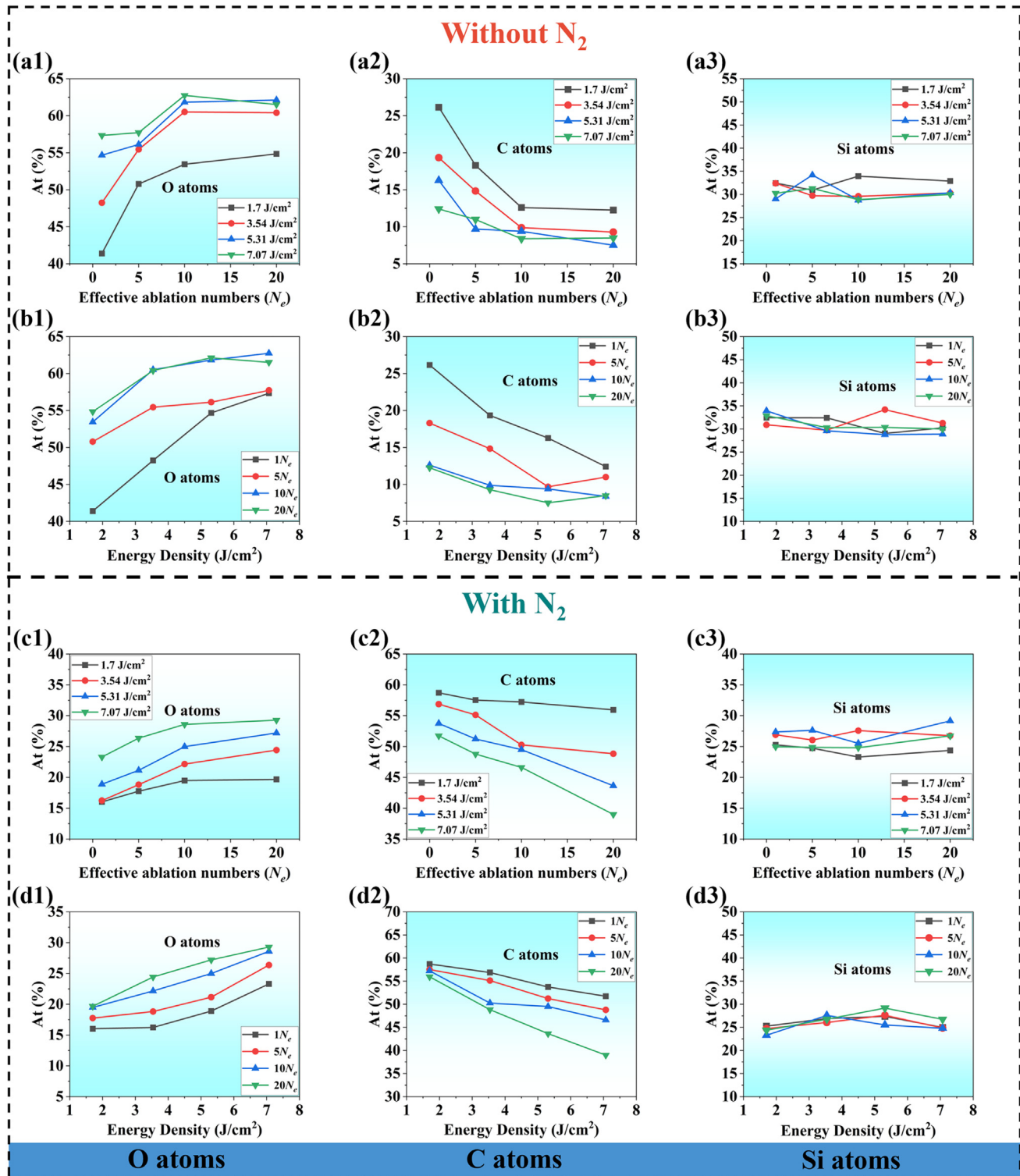


Fig. 7 – The statistical plot of the EDS surface scans for each ablation location corresponds to Fig. 3: (a1-b3)without N<sub>2</sub>, (c1-d3) with N<sub>2</sub>.

decrease in the atomic ratio of C was caused by the escape of CO<sub>2</sub> or CO gas from SiC and PyC oxidation. This result was consistent with the analysis results of XPS. The reason for the relatively stable atomic ratio of Si was that Si atoms were present in both SiC, Si, and SiO<sub>2</sub>, and most of the SiO<sub>2</sub> and

other Si-containing solid products would be deposited near the ablation locations after laser processing.

Comparing the atomic ratio of C and O for the same parameters of the two groups of samples demonstrated again that N<sub>2</sub> could effectively inhibit the oxidation of the material.

The SiC, Si, and C oxidation temperatures were about 800 °C, 300 °C, and 450 °C, respectively [41]. It can be inferred that the temperature caused by the heat accumulation effect at each ablation location of both groups of samples might have exceeded 800 °C, combined with the above analytical results.

The above physical phase, morphology, structure, and composition analysis resulted from static detection before and after femtosecond laser ablation. However, in order to have a more comprehensive understanding of the dynamic evolution process of multi-pulse femtosecond laser ablation of SiC/SiC composites, this investigation examined the state of the plasma generated during the ablation process *in situ* with the aid of a high-speed plasma spectrometer. The oxidation behavior and removal mechanism of SiC/SiC composites ablated by femtosecond laser were further studied by information from plasma spectra.

**Fig. 8** shows the results of plasma spectra produced by a multi-pulse femtosecond laser on both groups of samples at different process parameters. Firstly, as shown in **Fig. 8(a)**, on the first group sample, the plasma discrete peaks mainly appeared at 187.5 nm, 192.3 nm, 378.5 nm, 387.7 nm, and 464.9 nm when the energy density was 1.77 J/cm<sup>2</sup>, and the peak intensities were gradually increased with the increase of the effective ablation number. The spectroscopic information tabulated in NIST Atomic Spectral Database [42] shows that the above plasma discrete peaks correspond to SiI, CIII, OII, CII, and OII, respectively. The I, II, and III represent neutral atoms, ions that have lost one electron and ions that have lost two electrons, respectively. The results illustrated that femtosecond laser ablation caused the SiC/SiC composites to be excited for plasmonization, which in turn removed the

material at the ablation location from the sample, mainly in the form of plasma. The final product at the ablation location was primarily a plasma deposit, but it is not excluded that the plasma oxidized during and after deposition. This material removal mechanism could be referred to as non-thermal removal.

As shown in **Fig. 8(b)**, on the first group sample, when the energy density reaches 3.54 J/cm<sup>2</sup>, a large number of other plasma peaks corresponding to C and O ions appear in the plasma spectra in addition to having the plasma peaks in **Fig. 8(a)**. It is shown that the high energy density will stimulate the production of more plasma. In particular, when the effective ablation number reached 10N<sub>e</sub>, there was a significant plasma continuum peak. According to relevant studies [43], this was because of the generation of high-temperature plasma. When high-temperature plasma was present, in addition to participating in the plasmaization of the material, the laser energy might be used for heat transfer in the material and even to cause heat accumulation at the ablation locations, which led to the material being removed from the sample by melting. This material removal mechanism could be referred to as thermal removal. Combined with the ablation results in **Fig. 3(b3)**, the occurrence of thermal removal was verified by significant recasts at the ablation location when the effective ablation number reached 10N<sub>e</sub>. The intensity of each peak decreased significantly when the effective ablation number increased to 20N<sub>e</sub>, which could be attributed to the plasma shielding effect. According to **Fig. 8(a–d)**, it could be seen that in the first group sample, the plasma peaks at different effective ablation numbers showed a similar trend when the energy density continued to increase, which ultimately

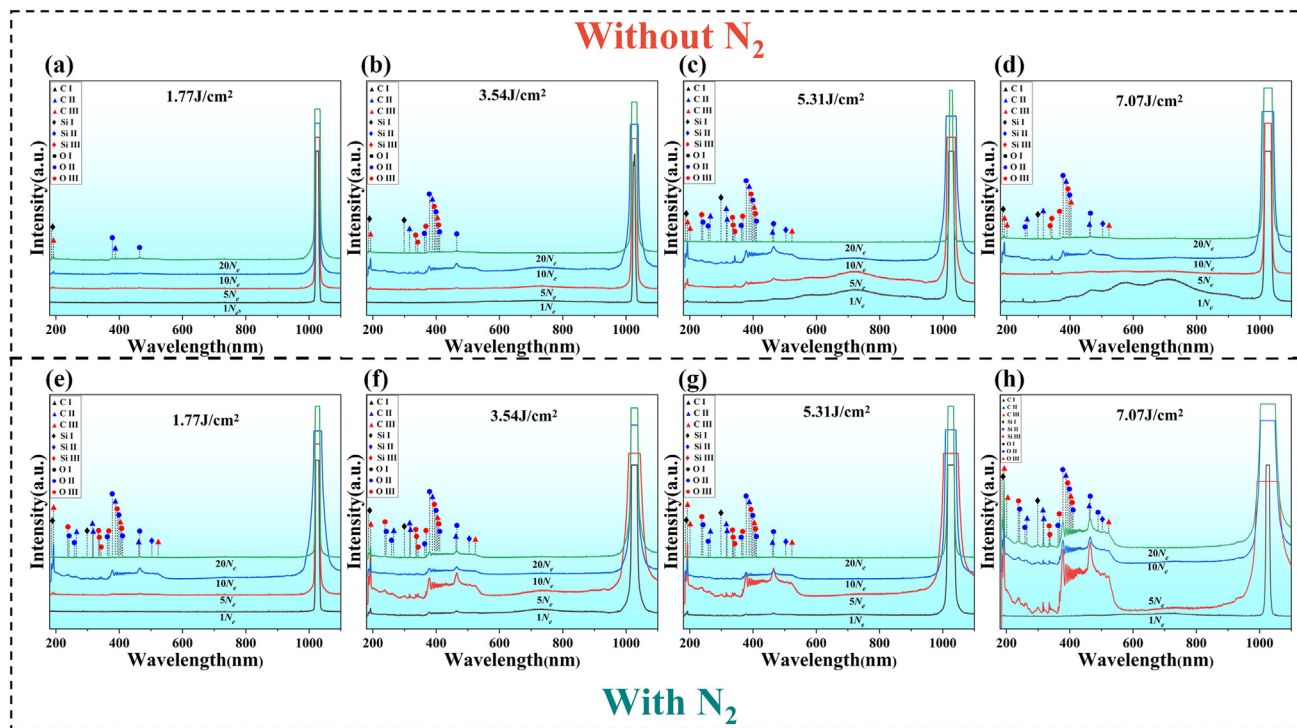


**Fig. 8 –** Plasma spectra results by multi-pulse femtosecond laser processing on two groups of SiC/SiC composite samples under different effective ablation numbers and energy densities: (a–d) without N<sub>2</sub>, (e–h) with N<sub>2</sub>.

resulted in a shift in the removal mechanism of the material from non-thermal removal to thermal removal as the effective ablation or energy density increased. This view was consistent with the analytical results in Fig. 3(a1-d4).

As shown in Fig. 8(a–h), the intensity of the plasma peaks corresponding to Si, C, and O on the second group sample increased significantly relative to the state of the plasma peaks on the first group sample at each process parameter. This showed that under the same laser energy input to the SiC/SiC composites, the use of 1 MPa N<sub>2</sub> significantly enhanced the material to undergo plasmonization, thus inhibiting the participation of the laser energy in heat accumulation, and ultimately prevented the material removal mechanism dominated by thermal removal. Moreover, it was further verified that different degrees of laser energy were involved in heat accumulation in the first group sample, leading to the material removal mechanism dominated by thermal removal.

The SEM images of typical morphologies of the raw material and ablation locations are shown in Fig. 9 (a1-b4). Fig. 9

(c1-d4) show the EDS surface scans of the raw material and the EDS point scans of the seven points selected in the SEM images. Fig. 9(a2) showed the flocculent at the initial stage of multi-pulse femtosecond laser ablated the SiC/SiC composites. Fig. 9(c2) corresponded to the EDS results of the flocculent (EDS-1) in Fig. 9(a2). A comparison with the atomic ratio of Si, O, and C in the raw material showed that the main component of the flocculent was SiO<sub>2</sub>, and there might be Si, O, and C-containing plasma deposits resulting from non-thermal removal. As shown in Fig. 9(a3), when the effective ablation number or energy density was increased, the ablation locations showed significant particulate and fibrous products in addition to the original flocculent. Fig. 9(c3,c4,d1) corresponded to the EDS results of flocculent (EDS-2), particle (EDS-3), and fiber (EDS-4) in Fig. 9(a3), respectively. As could be seen from the figure, the flocculent in Fig. 9(a3) and Fig. 9(a2) had the same composition, and the composition of the particulate and fibrous products were similar, both being mainly SiO<sub>2</sub>. Moreover, the particulate and fibrous products were more oxidized than the flocculent. As shown in Fig. 9(a4), when the

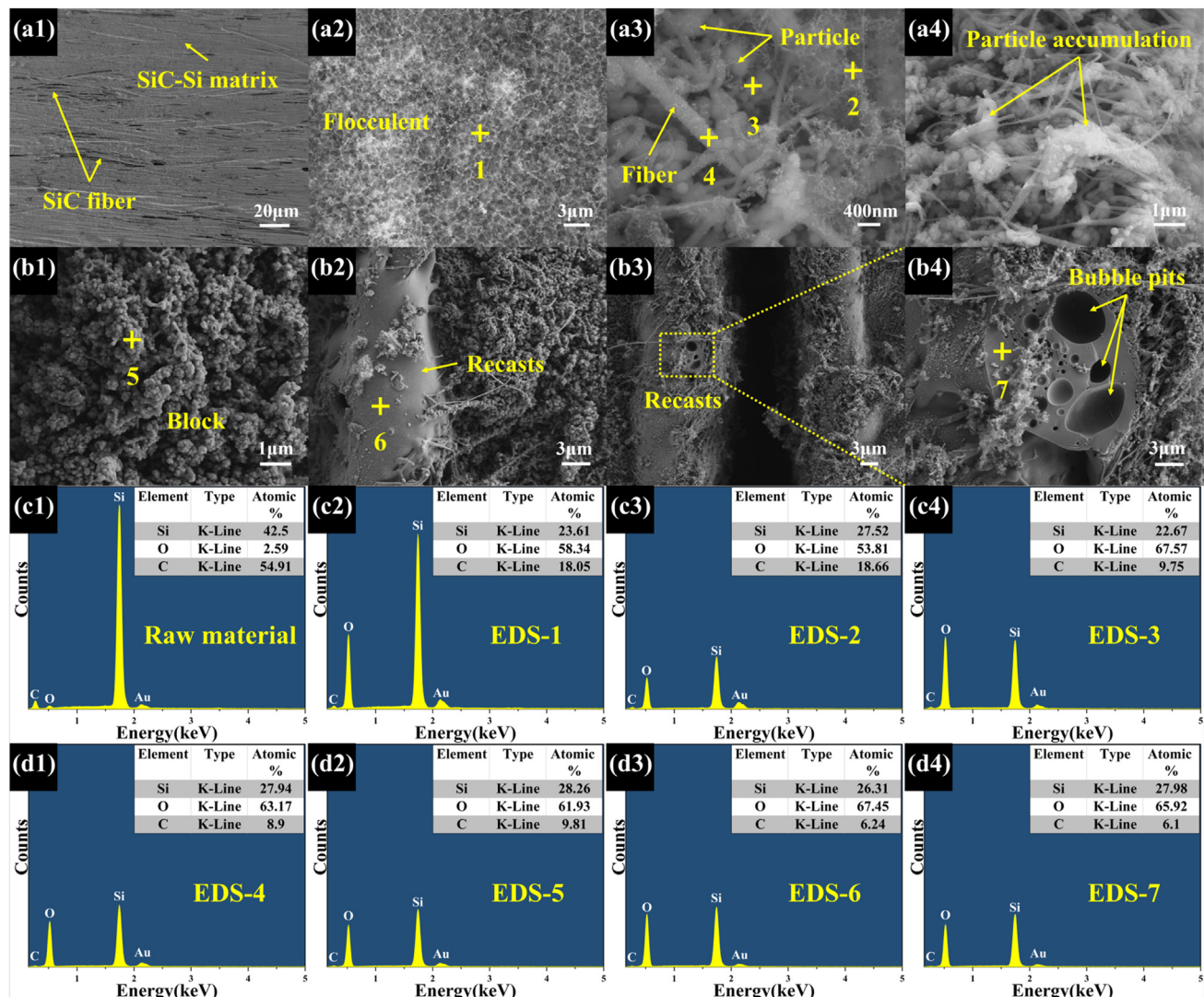


**Fig. 9 – (a1-b4)** SEM images of typical morphologies of the raw material and ablation locations. **(c1-d4)** EDS surface scans of the raw material and the EDS point scans of the seven points selected in the SEM images.

effective ablation number or energy density was further increased, the volume of the particle increased and adhered to the fibrous products in a large amount, and the main shape of the products became block, as shown in Fig. 9(b1). Fig. 9(d2) corresponded to the EDS results of the blocks (EDS-5) in Fig. 9(b2), which showed that the blocks had the same composition as the particulate and fibrous products, again mainly  $\text{SiO}_2$ .

The main shape of the above products was a common situation in both groups of samples. Other than that, as shown in Fig. 9(b2), when the effective ablation number or energy density increased to a certain extent, recasts due to thermal removal appeared on the edge of the grooves at the first group sample without the  $\text{N}_2$ . Fig. 9(d3,d4) corresponded to the EDS results of the surface (EDS-6) and the interior (EDS-7) of the recasts in Fig. 9(b2,b4), respectively, which showed that the composition of the recast was relatively homogeneous. In addition, the ratios of Si and O at both detected positions were close to 1:2, indicating that the main component of the recast was  $\text{SiO}_2$ . Moreover, many bubble pits with a diameter of about 0.1–7.5  $\mu\text{m}$  exist inside the recasts, which might be caused by  $\text{CO}_2$ ,  $\text{CO}$ , and  $\text{SiO}$  gases generated by the oxidation of  $\text{SiC}$  and C. Combining the analyzed results in Figs. 3 and 7, it was clear that the enhanced heat accumulation effect raised the temperature at the ablation locations, which caused the aggregation of the  $\text{SiO}_2$  and even led to the transformation of its main shape. Therefore, the recasts were formed due to the heat accumulation effect resulting in high temperature,

eventually melting the generated  $\text{SiO}_2$ , and the molten  $\text{SiO}_2$  along the groove wall or splash moved to the edge of the groove. Meanwhile, the material removal mechanism was dominated by thermal removal. Since the gas generated by the reaction of each component would overflow into the air through the interior of molten  $\text{SiO}_2$ , many bubble pits appeared inside the recasts when the molten  $\text{SiO}_2$  solidified.

Fig. 10(a–d) show the SEM images of the typical morphologies of the groove wall when the energy density was 1.77  $\text{J}/\text{cm}^2$  with different effective ablation numbers in the first group sample. As shown in the figure, when the effective ablation was  $1N_e$ , the groove wall was mainly covered by flocculent, and the surface showed a relatively smooth trend. At this time, the removal mechanism of  $\text{SiC}/\text{SiC}$  composites was dominated by non-thermal removal, and the products were mainly  $\text{SiO}_2$  and plasma deposits resulting from the excitation of the material by laser irradiation. When the effective ablation number was increased to  $5N_e$ , the surface of the groove wall appeared folded, and its flatness decreased. The folding phenomenon could be attributed to the accumulation of large amounts of  $\text{SiO}_2$  and plasma deposits while the thermal removal mechanism was gradually enhanced. When the effective ablation number continued to increase to  $10N_e$ , the flocculent on the groove wall underwent serious collapse, forming many shallow holes and blocks, and there was a tendency to form heavy recasts. At this stage, the thermal removal gradually became prominent, resulting in the collapse of the products on the groove wall due to heat

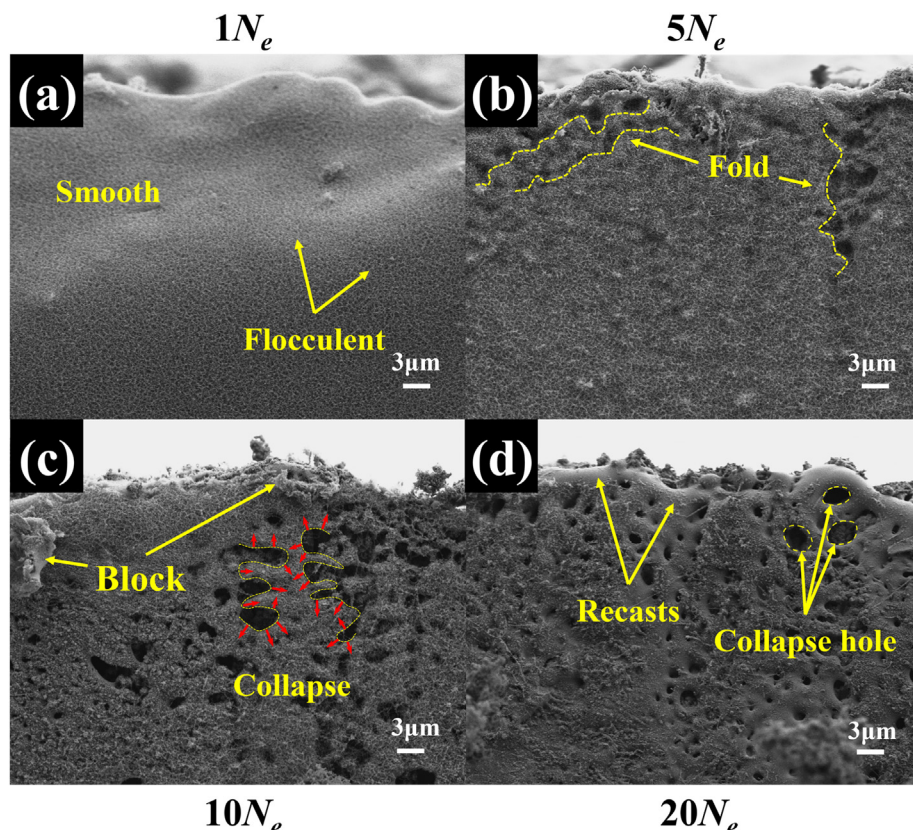


**Fig. 10 – SEM images of typical morphologies of the groove wall when the energy density was 1.77  $\text{J}/\text{cm}^2$  in the first group sample: (a)  $1N_e$ , (b)  $5N_e$ , (c)  $10N_e$ , (d)  $20N_e$ .**

accumulation. However, the thermal removal was in equilibrium with the non-thermal removal. When the effective ablation number increased to  $20N_e$ , the surface of the groove wall was covered by significant recasts, and many collapsed holes with diameters less than  $8\text{ }\mu\text{m}$  were formed. At the same time, there was little residual flocculent and block. The results showed that the morphology of the ablation products had changed from flocculent and block to recasts due to the heat accumulation effect, and the removal mechanism of SiC/SiC composites was dominated by thermal removal at this time. Combined with the results of the above analysis, the typical morphology at this group of parameters could represent the change process of the main shape of the products at the ablation positions. The upper part of Fig. 13 shows a schematic diagram of the change process of the main shape of the femtosecond laser ablation products in this study.

Combined with the study of Li et al. [44], it was known that the surface of SiC/SiC composites without ablation formed dense and stable  $\text{SiO}_2$  films due to weak oxidation, which prevented the material from further oxidation and improved the mechanical properties and service life of SiC/SiC composite components to some extent. In structures such as holes and grooves of SiC/SiC composites, if a dense, homogeneous, and strong bonding  $\text{SiO}_2$  recasts layer was ablated on the hole and groove walls as a protective coating using the femtosecond laser, the exposure of the pores and cross-sections of the fibers to air would be avoided, thus reducing the oxidation and damage of the structural components in service and ultimately improving its performance under special requirements. Therefore, this is an important direction that we need to study further.

The relative strengths of the thermal and non-thermal removal mechanisms in this study were roughly represented by estimating the volume percent of recasts at the ablation locations for each process parameter in Fig. 3. As shown in Fig. 11, the removal mechanism of femtosecond laser ablation of SiC/SiC composites in this study could be categorized into

non-thermal removal dominated (Stage 1), equilibrium (Stage 2), and thermal removal dominated (Stage 3). The removal mechanism of the femtosecond laser ablation of SiC/SiC composites was at stages 1 and 2 under the process parameters of using 1 MPa  $\text{N}_2$ . Without  $\text{N}_2$ , the removal mechanism included stages 1, 2, and 3. Therefore, in this study, to avoid thermal removal as dominant to produce defects such as recasts and bubble pits. On the one hand, when using 1 MPa  $\text{N}_2$ , select the process parameters with an energy density not exceeding  $7.07\text{ J/cm}^2$  and an effective ablation number not exceeding  $20N_e$ . On the other hand, without  $\text{N}_2$ , the energy density was selected not to exceed  $7.07\text{ J/cm}^2$  at an effective ablation number of  $1N_e$ , and the effective ablation number was selected not to exceed  $10N_e$  at an energy density of  $1.77\text{ J/cm}^2$ .

Due to the ultra-short pulse width ( $10^{-15}\text{ s}$ ) of the femtosecond laser, which is much smaller than the electron-lattice relaxation time ( $10^{-10} \sim 10^{-12}\text{ s}$ ), and the ultra-high peak power, the femtosecond laser can break the diffraction limit during ablate material and inject ultra-high instantaneous power into extremely small ablation regions in an ultra-short time [45–49]. After that, the material undergoes multiphoton nonlinear absorption [50] followed by complex nonlinear ionization [51,52] and then removes the material in an extremely small region, mainly in the form of plasma. Compared to long pulse lasers, femtosecond lasers greatly limit the thermal effects.

In combination with the above theories, the SiC/SiC composites mainly contain Si–C, Si–Si, and C–C chemical bonds with bond energies of 347 kJ/mol, 176 kJ/mol, and 332 kJ/mol, respectively, and the corresponding photon energies of 3.61 eV, 1.83 eV, and 3.45 eV. The single photon energy of the 1030 nm wavelength femtosecond laser used in this study was 1.2 eV, and the energy through multiphoton nonlinear absorption by the material was sufficient to break the stable Si–Si, Si–C, and C–C bonds. Therefore, when the multi-pulse femtosecond laser irradiated the SiC/SiC composites, the crystal structure of each component on the material was destroyed first. The ultra-high instantaneous power of the femtosecond laser at the ablation center caused Si–Si, Si–C, and C–C bonds to break, resulting in the components being stripped from the material, mainly in the form of plasma. However, the heat accumulation effect led to the oxidation of SiC, Si, and C in an environment with oxygen, regardless of whether they were stripped from the material. As shown in Eqs. (2)–(4), the oxidation behavior of Si and C is relatively simple.



However, the oxidation behavior of SiC, which is the main component of the fiber and matrix, is more complex. Fig. 12 shows the relationship between the oxidation behavior of SiC and the oxygen partial pressure and the temperature, which results from several mechanisms together, with different mechanisms dominating under different conditions [20,53]. As shown in Eqs. (5)–(8), which include passive

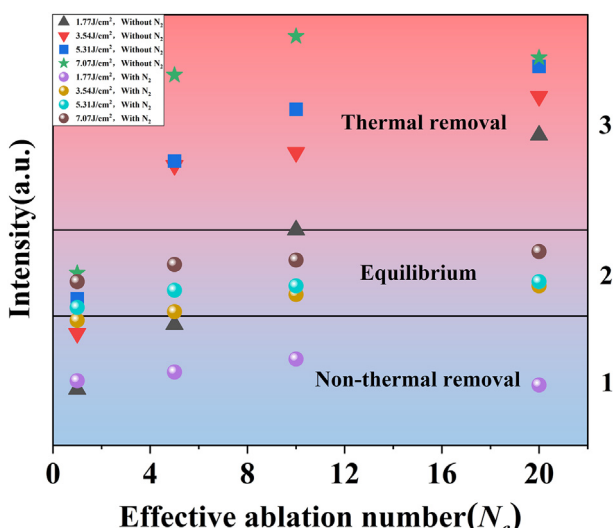
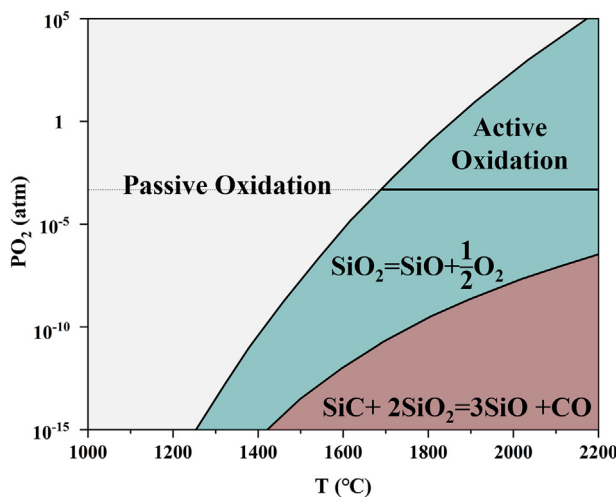
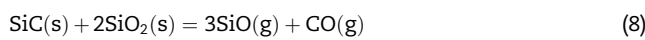
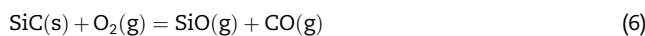
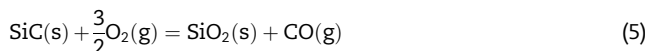


Fig. 11 – Relative strengths of removal mechanism under femtosecond laser ablated SiC/SiC composites with different process parameters.



**Fig. 12 – Relationship between the oxidation behavior of SiC and the oxygen partial pressure and the temperature [20,53].**



oxidation of SiC, active oxidation of SiC, volatilization of SiO<sub>2</sub>, and reaction decomposition of SiC with SiO<sub>2</sub>, respectively [20,53]. Of these, the active oxidation of SiC required SiC to react with atmospheric oxygen at high temperatures. Therefore, combined with Fig. 12, it could be seen that for the first group sample in atmospheric air, the heat accumulation effect caused a gradual increase in temperature with the increase in the effective ablation number or energy density, which eventually led to a gradual change in the dominant mechanism of the oxidation behavior of SiC at the ablation locations from passive oxidation of SiC to active oxidation of SiC. For the second group sample using N<sub>2</sub>, the 1 MPa N<sub>2</sub> caused an extremely low oxygen partial pressure at the ablation locations. The heat accumulation effect and temperature were gradually enhanced with the increase of the effective ablation number or energy density, which eventually led to the change of the dominant mechanism at the ablation locations from passive oxidation of SiC to volatilization of SiO<sub>2</sub> and then to the reaction decomposition of SiC and SiO<sub>2</sub>. This was one reason less SiO<sub>2</sub> was produced at the ablation locations when nitrogen was used.

Fig. 13 shows the schematic diagram of the change process of the main shape of the femtosecond laser ablation products and the dominant oxidation behavior on the SiC/SiC composites in this study. However, a more comprehensive interaction mechanism between the femtosecond laser and SiC/SiC composites at the atomic level still needs further refinement by subsequent work. The above studies on the oxidation behavior and removal mechanism of multi-pulse femtosecond laser ablation of SiC/SiC composites have important guiding significance for the practical engineering applications of the femtosecond laser and SiC/SiC composites.

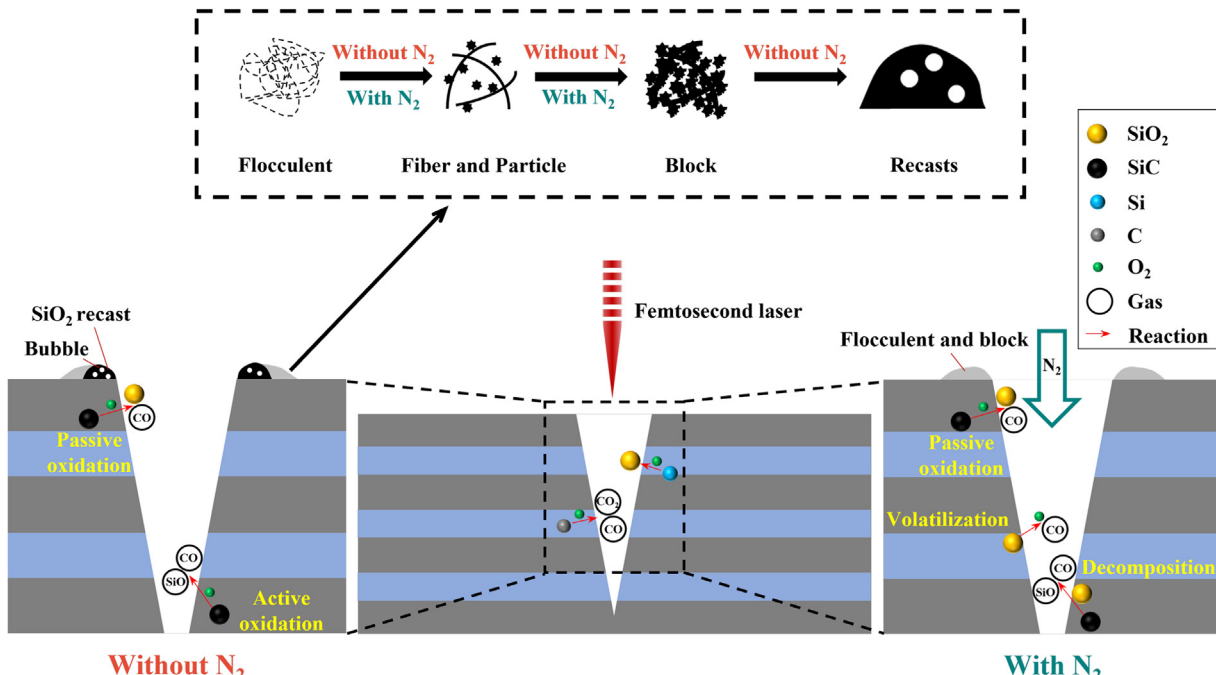


**Fig. 13 – Schematic diagram of the change process of the main shape of the products and the dominant oxidation behavior on the SiC/SiC composites.**

## 4. Conclusions

In this paper, the morphology, structure, composition, and plasma state of 2D SiC/SiC composites ablated by a multi-pulse femtosecond laser at a wavelength of 1030 nm were analyzed in detail from several perspectives. The oxidation behavior and removal mechanism of multi-pulse femtosecond laser ablation of SiC/SiC composites were qualitatively and quantitatively investigated. The following conclusions can be drawn.

- (1) The ablation products of multi-pulse femtosecond laser ablation of SiC/SiC composites were mainly  $\text{SiO}_2$  and plasma deposits. As the effective ablation number or energy density increased, the main shape of the products gradually changed from flocculent to particle and fiber, after which it became the block and eventually formed  $\text{SiO}_2$  recasts. Using  $\text{N}_2$  could effectively inhibit the heat accumulation effect at the ablation locations and the oxidation of SiC, Si, and C, thus avoiding the generation of recasts and improving the processing efficiency and capability of the femtosecond laser. In this investigation, 1 MPa  $\text{N}_2$  could improve the processing efficiency of femtosecond laser for the depth and width of the groove by a maximum of about 90.40% and 104.02%, respectively.
- (2) During this investigation, the heat accumulation effect and oxidation degree at the ablation locations were enhanced accordingly as the effective ablation number or energy density increased. At the same time, the material removal mechanism changed from non-thermal removal dominated to the equilibrium stage and then to thermal removal dominated. The following process parameters could be selected to avoid producing defects such as recasts and bubble pits due to thermal removal. On the one hand, when using 1 MPa  $\text{N}_2$ , select the process parameters with an energy density not exceeding 7.07 J/cm<sup>2</sup> and an effective ablation number not exceeding 20 $N_e$ . On the other hand, without  $\text{N}_2$ , the energy density was selected not to exceed 7.07 J/cm<sup>2</sup> at an effective ablation number of 1 $N_e$ , and the effective ablation number was selected not to exceed 10 $N_e$  at an energy density of 1.77 J/cm<sup>2</sup>.
- (3) In this investigation, the SiC/SiC composites were oxidized to a certain extent under different femtosecond laser process parameters, and the oxidation behaviors of each component were significantly different. Si and C oxidized to form oxides such as  $\text{SiO}_2$ ,  $\text{CO}_2$ , and CO, respectively. However, the oxidation behavior of SiC was more complicated. As the gradual increase of the effective ablation number or energy density, the dominant mechanism of the oxidation behavior of SiC at the ablation locations gradually changed from passive oxidation of SiC to active oxidation of SiC when no  $\text{N}_2$  was used. When 1 MPa  $\text{N}_2$  was used, the dominant mechanism of the oxidation behavior at the ablation locations changed from passive oxidation of SiC to volatilization of  $\text{SiO}_2$  to the reaction decomposition of SiC and  $\text{SiO}_2$ .

## Author contributions

**Ning Zhou:** conceptualization, investigation, visualization, methodology, formal analysis, data curation, writing-original draft, writing-review and editing, validation. **Songmei Yuan:** funding acquisition, writing-review and editing, supervision. **Mengxuan Gao:** writing-review and editing. **Wei Zhang:** conceptualization, investigation. **Jiaqi Zhang:** investigation. **Tianrui Hu:** investigation.

## Declaration of competing interest

The authors declare that they have no known competing financial interests or personal relationships that could have appeared to influence the work reported in this paper.

## Acknowledgments

This work was supported by Science Center for Gas Turbine Project (P2022-A-IV-002-002).

## REFERENCES

- [1] Chen G, Peng YB, Zheng G, Qi ZX, Wang MZ, Yu HC, et al. Polysynthetic twinned TiAl single crystals for high-temperature applications. *Nat Mater* 2016;15(8):876–81. <https://doi.org/10.1038/nmat4677>.
- [2] Fellah C, Braun J, Sauder C, Sirotti F, Berger M-H. Influence of the carbon interface on the mechanical behavior of SiC/SiC composites. *Compos. Part A-Appl S* 2020;133:105867. <https://doi.org/10.1016/j.compositesa.2020.105867>.
- [3] Padture NP. Advanced structural ceramics in aerospace propulsion. *Nat Mater* 2016;15(8):804–9. <https://doi.org/10.1038/nmat4687>.
- [4] Shi DQ, Zhang B, Liu CQ, Wang LY, Yang XG, Luo RY. In-situ study on compressive behaviors of different types of 3D SiC/SiC composites using X-ray computed tomography and digital image correlation. *J Mater Res Technol* 2023;22:3475–88. <https://doi.org/10.1016/j.jmrt.2022.12.178>.
- [5] Yang J, Zhang XY, Ma GL, Lin PP, Xu YQ, Liu ZG, et al. A study of the SiC<sub>f</sub>/SiC composite/Ni-based superalloy dissimilar joint brazed with a composite filler. *J Mater Res Technol* 2021;11:2114–26. <https://doi.org/10.1016/j.jmrt.2021.01.081>.
- [6] Liu YS, Wang J, Li WN, Wang CH, Zhang Q, Yang XJ, et al. Effect of energy density and feeding speed on micro-holes drilling in SiC/SiC composites by picosecond laser. *Int J Adv Manuf Technol* 2016;84:1917–25. <https://doi.org/10.1007/s00170-015-7844-1>.
- [7] Xiong YF, Wang WH, Jiang RS, Huang B, Liu C. Feasibility and tool performance of ultrasonic vibration-assisted milling-grinding SiC<sub>f</sub>/SiC ceramic matrix composite. *J Mater Res Technol* 2022;19:3018–33. <https://doi.org/10.1016/j.jmrt.2022.06.063>.
- [8] Kovacevic R, Hashish M, Mohan R, Ramulu M, Kim TJ, Geskin ES. State of the art of research and development in abrasive waterjet machining. *J Manuf Sci Eng* 1997;119(4B):776–85. <https://doi.org/10.1115/1.2836824>.
- [9] Li ZC, Jiao Y, Deines TW, Pei ZJ, Treadwell C. Rotary ultrasonic machining of ceramic matrix composites:

- feasibility study and designed experiments. *Int J Mach Tool Manufact* 2005;45:1402–11. <https://doi.org/10.1016/j.ijmachtools.2005.01.034>.
- [10] Yang Y, Zhao Y, Wang LK, Zhao YL. Application of femtosecond laser etching in the fabrication of bulk SiC accelerometer. *J Mater Res Technol* 2022;17:2577–86. <https://doi.org/10.1016/j.jmrt.2022.02.012>.
- [11] Zhai ZY, Wei C, Zhang YC, Cui YH, Zeng QR. Investigations on the oxidation phenomenon of SiC/SiC fabricated by high repetition frequency femtosecond laser. *Appl Surf Sci* 2020;502:144131. <https://doi.org/10.1016/j.apsusc.2019.144131>.
- [12] Liu YS, Zhang RH, Li WN, Wang J, Yang XJ, Cheng LF, et al. Effect of machining parameter on femtosecond laser drilling processing on SiC/SiC composites. *Int J Adv Manuf Technol* 2018;96(5):1795–811. <https://doi.org/10.1007/s00170-017-1163-7>.
- [13] Yan ZX, Lin QY, Li GJ, Zhang Y, Wang WJ, Mei XS. Femtosecond laser polishing of SiC/SiC composites: effect of incident angle on surface topography and oxidation. *J Compos Mater* 2021;55(11):1437–45. <https://doi.org/10.1177/0021998320972175>.
- [14] Liu B, Yan YJ, Zhao J, Wang WJ, Liao K. Research on hole depth in femtosecond laser deep micropore processing technology based on filament effect. *Optik* 2022;249:168307. <https://doi.org/10.1016/j.jleo.2021.168307>.
- [15] Wang WJ, Mei XS, Jiang GD. Control of microstructure shape and morphology in femtosecond laser ablation of imprint rollers. *Int J Adv Manuf Technol* 2009;41:504–12. <https://doi.org/10.1007/s00170-008-1490-9>.
- [16] Li ZJ, Zhao J, Zhang M, Xia JY, Meng A. SiC nanowires with thickness-controlled SiO<sub>2</sub> shells: fabrication, mechanism, reaction kinetics and photoluminescence properties. *Nano Res* 2014;7(4):462–72. <https://doi.org/10.1007/s12274-014-0413-3>.
- [17] Tateyama H, Noma H, Adachi Y, Komatsu M. Prediction of stacking faults in  $\beta$ -silicon carbide: X-ray and NMR studies. *Chem Mater* 1997;9(3):766–72. <https://doi.org/10.1021/cm960471d>.
- [18] Zhang Y, Jiang YZ, Li YD, Li BB, Li ZH, Niu CM. Preparation of nanographite sheets supported Si nanoparticles by in situ reduction of fumed SiO<sub>2</sub> with magnesium for lithium ion battery. *J Power Sources* 2015;281:425–31. <https://doi.org/10.1016/j.jpowsour.2015.02.020>.
- [19] Liu YS, Cheng LF, Zhang LT, Wu SJ, Li D, Xu YD. Oxidation protection of multilayer CVD SiC/B/SiC coatings for 3D C/SiC composite. *Mat. Sci. Eng. A-Struct.* 2007;466:172–7. <https://doi.org/10.1016/j.msea.2007.02.059>.
- [20] Chen J, An QL, Ming WW, Chen M. Investigations on continuous-wave laser and pulsed laser induced controllable ablation of SiC<sub>f</sub>/SiC composites. *J Eur Ceram Soc* 2021;12(41):5835–49. <https://doi.org/10.1016/j.jeurceramsoc.2021.04.061>.
- [21] Cai M, Zhang XB, Zhang W, Ji L, Jiao JN, Qiu HP. Study on quality of holes in SiC/SiC composites with nanosecond laser and picosecond laser drilling. *Aeronaut. Manuf. Technol.* 2016;19:52–5. <https://10.16080/j.issn1671-833x.2016.19.052>.
- [22] Eaton SM, Zhang HB, Ng ML, Li JZ, Chen WJ, Ho S, et al. Transition from thermal diffusion to heat accumulation in high repetition rate femtosecond laser writing of buried optical waveguides. *Opt Express* 2008;16(13):9443–58. <https://doi.org/10.1364/OE.16.009443>.
- [23] Richter S, Döring S, Burmeister F, Zimmermann F, Tünnermann A, Nolte S. Formation of periodic disruptions induced by heat accumulation of femtosecond laser pulses. *Opt Express* 2013;21(13):15452–63. <https://doi.org/10.1364/OE.21.015452>.
- [24] Guk I, Shandybina G, Yakovlev E. Influence of accumulation effects on heating of silicon surface by femtosecond laser pulses. *Appl Surf Sci* 2015;353:851–5. <https://doi.org/10.1016/j.apsusc.2015.05.195>.
- [25] Sulistyo J, Hata T, Kitagawa H, Bronsveld P, Fujisawa M, Hashimoto K, et al. Electrical and thermal conductivities of porous SiC/SiO<sub>2</sub>/C composites with different morphology from carbonized wood. *J Mater Sci* 2010;45:1107–16. <https://doi.org/10.1007/s10853-009-4053-z>.
- [26] Zhang W, Zhang S, Liu Y, Chen T. Evolution of Si suboxides into Si nanocrystals during rapid thermal annealing as revealed by XPS and Raman studies. *J Cryst Growth* 2009;311:1296–301. <https://doi.org/10.1016/j.jcrysgr.2008.12.038>.
- [27] Wang J, Liu Y, Wang C, Li W, Yang X, Zhang Q, et al. Character and mechanism of surface micromachining for C/SiC composites by ultrashort plus laser. *Adv Appl Ceram* 2017;116(2):99–107. <https://doi.org/10.1080/17436753.2016.1257101>.
- [28] Zhai ZY, Wu NQ, Wang ZL, Zhang YF, Song DL, Cui YH. Fabrication of LiG coating on SiC/SiC composites with femtosecond laser. *Optik* 2021;245:167628. <https://doi.org/10.1016/j.jle.2021.167628>.
- [29] Liu M, Yang XM, Gao YT, Liu RD, Huang HF, Zhou XT, et al. Investigation of the damage behavior in CVD SiC irradiated with 70 keV He ions by NEXAFS, Raman and TEM. *J Eur Ceram Soc* 2017;37(4):1253–9. <https://doi.org/10.1016/j.jeurceramsoc.2016.11.046>.
- [30] Fu CL, Yang Y, Huang ZR, Liu GL, Zhang H, Jiang F, et al. Investigation on the laser ablation of SiC ceramics using micro-Raman mapping technique. *J. Adv. Ceram.* 2016;5(3):253–61. <https://doi.org/10.1007/s40145-016-0197-x>.
- [31] Zhong B, Kong LQ, Zhang B, Yu YL, Xia L. Fabrication of novel hydrophobic SiC/SiO<sub>2</sub> bead-string like core-shell nanochains via a facile catalyst/template-free thermal chemical vapor deposition process. *Mater Chem Phys* 2018;217:111–6. <https://doi.org/10.1016/j.matchemphys.2018.06.043>.
- [32] Liu GZ, Wang FH, Su GW, Wang W, Wei HY, Dang LP. Novel synthesis of SiC/SiO<sub>2</sub> nanochain heterojunctions from agricultural waste. *Ceram Int* 2022;48(9):13229–36. <https://doi.org/10.1016/j.ceramint.2022.01.200>.
- [33] Gao L, Zhong H, Chen QW. Synthesis of 3C-SiC nanowires by reaction of poly(ethylene terephthalate) waste with SiO<sub>2</sub> microspheres. *J Alloys Compd* 2013;566:212–6. <https://doi.org/10.1016/j.jallcom.2013.03.043>.
- [34] Wing BL, Halloran JW. Microstress in the matrix of a melt-infiltrated SiC/SiC ceramic matrix composite. *J Am Ceram Soc* 2017;100(11):5286–94. <https://doi.org/10.1111/jace.15038>.
- [35] Tang YH, Zhang YF, Peng HY, Wang N, Lee CS, Lee ST. Si nanowires synthesized by laser ablation of mixed SiC and SiO<sub>2</sub> powders. *Chem Phys Lett* 1999;314(1–2):16–20. [https://doi.org/10.1016/S0009-2614\(99\)01119-7](https://doi.org/10.1016/S0009-2614(99)01119-7).
- [36] Yapuchura ER, Tartaglia RS, Cunha AG, Freitas JCC, Emmerich FG. Observation of the transformation of silica phytoliths into SiC and SiO<sub>2</sub> particles in biomass-derived carbons by using SEM/EDS, Raman spectroscopy, and XRD. *J Mater Sci* 2019;54:3761–77. <https://doi.org/10.1007/s10853-018-3130-6>.
- [37] Tian H, Liu HT, Cheng HF. Effects of SiC contents on the dielectric properties of SiO<sub>2</sub>/SiO<sub>2</sub> composites fabricated through a sol-gel process. *Powder Technol* 2013;239:374–80. <https://doi.org/10.1016/j.powtec.2013.02.021>.
- [38] Qiang XF, Li HJ, Zhang YL, Tian S, Wei JF. Synthesis of SiC/SiO<sub>2</sub> nanocables by chemical vapor deposition. *J Alloys Compd* 2013;572:107–9. <https://doi.org/10.1016/j.jallcom.2013.03.268>.

- [39] Meng AL, Li ZJ, Zhang JL, Gao L, Li HJ. Synthesis and Raman scattering of  $\beta$ -SiC/SiO<sub>2</sub> core-shell nanowires. *J Cryst Growth* 2007;308(2):263–8. <https://doi.org/10.1016/j.jcrysgro.2007.08.022>.
- [40] Li ZJ, Gao WD, Meng AL, Geng ZD, Gao L. Large-scale synthesis and Raman and photoluminescence properties of single crystalline  $\beta$ -SiC nanowires periodically wrapped by amorphous SiO<sub>2</sub> nanospheres 2. *J Phys Chem C* 2009;113(1):91–6. <https://doi.org/10.1021/jp806346d>.
- [41] Zhang YH, Liu YS, Cao LY, Chen J, Qiu GT, Wang J. Preparation and analysis of micro-holes in C/SiC composites and ablation with a continuous wave laser. *J Eur Ceram Soc* 2021;41:176–84. <https://doi.org/10.1016/j.jeurceramsoc.2020.08.033>.
- [42] US Department of Commerce, N. NIST atomic spectra Database. 2015. <https://www.physics.nist.gov/PhysRefData/ASD/LIBS/libs-form.html>.
- [43] Russo RE, Mao XL, Liu HC, Yoo JH, Mao SS. Time-resolved plasma diagnostics and mass removal during single-pulse laser ablation. *Appl. Phys. A-Mater.* 1999;69(7):887–94. <https://doi.org/10.1007/s003390051553>.
- [44] Li WN, Zhang RH, Liu YS, Wang CH, Wang J, Yang XJ, et al. Effect of different parameters on machining of SiC/SiC composites via pico-second laser. *Appl Surf Sci* 2016;364:378–87. <https://doi.org/10.1016/j.apsusc.2015.12.089>.
- [45] Tan DZ, Sharafudeen KN, Yue YZ, Qiu JR. Femtosecond laser induced phenomena in transparent solid materials: fundamentals and applications. *Prog Mater Sci* 2016;76:154–228. <https://doi.org/10.1016/j.pmatsci.2015.09.002>.
- [46] Gamaly EG, Rode AV, Davies BL, Tikhonchuk VT. Ablation of solids by femtosecond lasers: ablation mechanism and ablation thresholds for metals and dielectrics. *Phys Plasmas* 2002;9:949–57. <https://doi.org/10.1063/1.1447555>.
- [47] Bonse J, Krüger J. Probing the heat affected zone by chemical modifications in femtosecond pulse laser ablation of titanium nitride films in air. *J Appl Phys* 2010;107(5):054902. <https://doi.org/10.1063/1.3311552>.
- [48] Konov VI. Laser in micro and nanoprocessing of diamond materials. *Laser Photon Rev* 2012;6(6):739–66. <https://doi.org/10.1002/lpor.201100030>.
- [49] Wu MT, Guo B, Zhao QL, He P, Zeng ZQ, Zang J. The influence of the ionization regime on femtosecond laser beam machining mono-crystalline diamond. *Opt Laser Technol* 2018;106:34–9. <https://doi.org/10.1016/j.optlastec.2018.03.031>.
- [50] Forster M, Huber C, Armbruster O, Kalish R, Kautek W. 50-nanometer femtosecond pulse laser induced periodic surface structures on nitrogen-doped diamond. *Diam Relat Mater* 2017;74:114–8. <https://doi.org/10.1016/j.diamond.2017.02.016>.
- [51] Sivakumar M, Tan B, Venkatakrishnan K. Enhancement of silicon nanostructures generation using dual wavelength double pulse femtosecond laser under ambient condition. *J Appl Phys* 2010;107(4):044307. <https://doi.org/10.1063/1.3309422>.
- [52] Ogawa Y, Ota M, Nakamoto K, Fukaya T, Russell M, Zohdi TI, et al. A study on machining of binder-less polycrystalline diamond by femtosecond pulsed laser for fabrication of micro milling tools. *CIRP Ann-Manuf. Techn.* 2016;65(1):245–8. <https://doi.org/10.1016/j.cirp.2016.04.081>.
- [53] Raj R, Terauds K. Bubble nucleation during oxidation of SiC. *J Am Ceram Soc* 2015;98(8):2579–86. <https://doi.org/10.1111/jace.13613>.